Supplementary Material to the Manuscript "Spin Properties of Very Shallow Nitrogen Vacancy Center in Diamond"

B. K. Ofori-Okai[1], S. Pezzagna[3], K. Chang[2], M. Loretz[2], R. Schirhagl[2], Y. Tao[1,2], B. A. Moores[2], K. Groot-Berning[3], J. Meijer[3], C. L. Degen[2]

[1]Department of Chemistry, Massachusetts Institute of Technology, 77 Massachusetts Avenue, Cambridge MA 02139, USA.

[2]Department of Physics, ETH Zurich, Schafmattstrasse 16, 8093 Zurich, Switzerland.

[3]RUBION, Ruhr-Universitaet Bochum, Universitaetsstrasse 150, 44780 Bochum, Germany.

1. Ion implantation and annealing

1.1. Ion implantation

Ion implantation was carried out with a 5 keV gas-source ion gun (SPECS) combined with a Wien mass filter (E×B). Ion beam direction was normal to the diamond surface [a (100) surface] with a precision of better than ±1°. Spot size was controlled by a 25 μm aperture. Fluence was measured via the ion current, and adjusted in a way that each spot received the same number of ions. Thus, even if spots slightly vary in shape, the number of ions impacting the larger area of the spot is the same. Miscalibration of the fluence is the largest error in the photoluminescence intensities presented in Fig. 1; in particular, it is most likely responsible for the low photoluminescence of the 1-keV row. Figure A shows a map of the implantation pattern, energies, and fluences that were used on the investigated sample. A detailed description of the ion implantation apparatus is given in Ref. [S1].

1.2. Annealing

Annealing was carried out in a AJA sputtering machine that allowed heating the diamond sample to 800°C while maintaining a pressure $< 2 \cdot 10^{-7}$ mbar over the entire annealing duration of 2h, followed by a slow overnight cool-down. It is assumed that this pressure is low enough to prevent oxidative etching of the top diamond layers. It is also assumed that nitrogen atoms do not diffuse under these conditions. Diffusion coefficients for N in diamond have been measured at higher temperatures in the context of geology [S2] and were found to follow an Arrhenius relationship,

$$D = 9.7 \cdot 10^{-8}\,\mathrm{m}^2/\mathrm{s}\; e^{\frac{-6.0\,\mathrm{eV}}{k_\mathrm{B} T}}. \tag{1}$$

At $T = 800\,^\circ$C, the diffusion coefficient is $D = 3 \cdot 10^{-35}\,\mathrm{m}^2/\mathrm{s}$. The diffusion length for this D and $t = 10^4$ s is $L = \sqrt{Dt} = 6 \cdot 10^{-16}$ m. This is much smaller than interatomic distances ($\sim 10^{-10}$ m). It is possible that the vacancies created around an implanted N atom will lower the activation energy for diffusion, however, such diffusion would be confined to the local area of the N defect and not significantly alter the N atoms's position.

1.3. Exclusion of near-surface ^{14}NV formation

There is a possibility that near-surface NV centers may be formed from native ^{14}N defects due to the vacancies created during ion implantation. A signature of such (unwanted) ^{14}NV formation would be an enhanced density of ^{14}NV centers on or near implantation spots. We have not observed

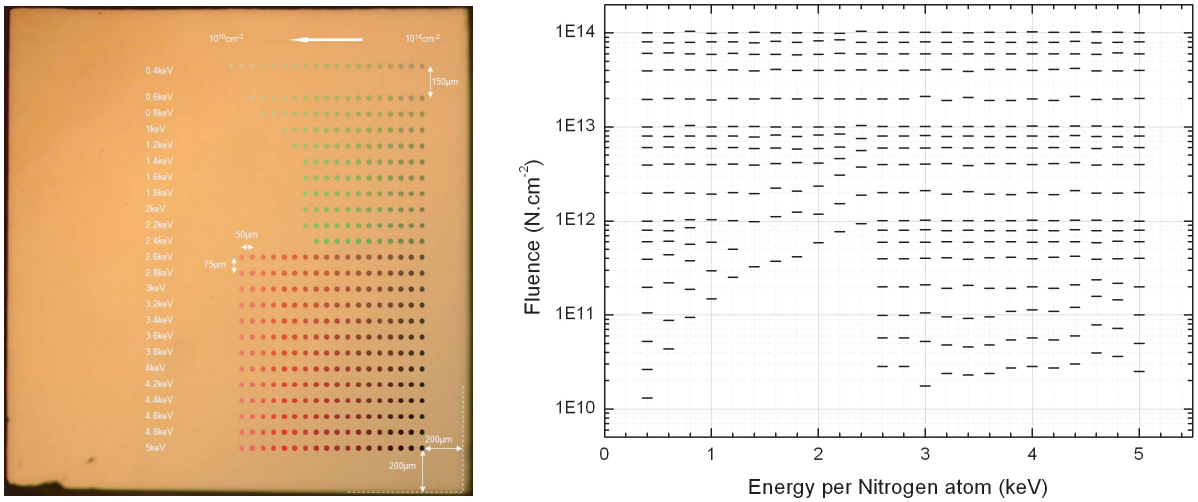

Figure A: (left) Spatial map of ion implantation. (right) Energies and fluences of the various spots.

such an increase with any of the implantation spots investigated by ODMR. From this we conclude that no significant number of near-surface NV centers is formed from native ^{14}N defects. This is plausible given the low intrinsic density of native ^{14}N of less than $<$ 5ppb [S3]. It is also in agreement with earlier studies on N implantation into diamond [S4].

2. Estimation of implantation depth for low energy ion implantation into diamond

The depth of defects created by ion implantation depends on the ion species, kinetic energy, and the target material. A widely used approach to calculate defect depth is the stopping range of ions in matter (SRIM) Monte Carlo simulation [S5]. It has been shown that SRIM simulations give suitable results of ion implantation depths over a wide energy range, including very low implantation energies [S6]. SRIM is the main approach used to estimate defect depths for our study. Figure B shows the calculated defect depth (peak depth) plotted against the ion energy for N ions in the range $0 - 5$ keV.

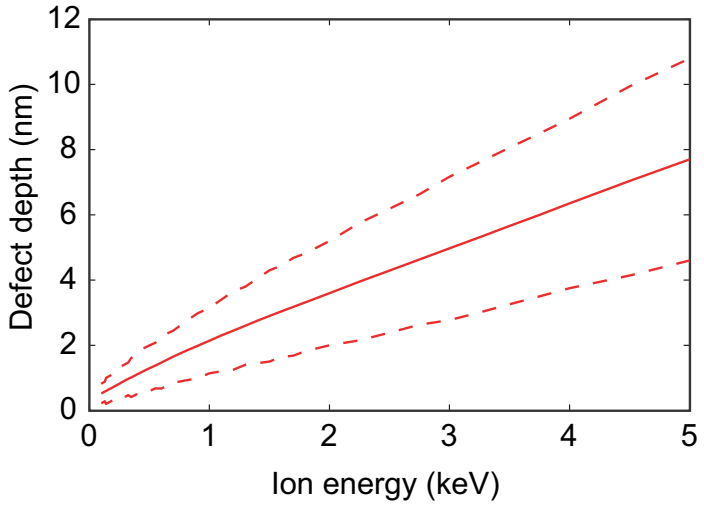

Figure B: SRIM Monte Carlo simulation for implantation of N ions into diamond. Solid line is peak depth (median) and dashed lines are ± 1 standard deviation.

The SRIM simulation does however not consider two potentially important effects that influence implantation depth, namely, aperture scattering and ion channeling. These effects are discussed in the following.

2.1. Aperture scattering

Proximity effects due to scattered ions on the mask are a well known problem in semiconductor industry. The scattered ions both reduce the lateral resolution and lead to a depth underestimation due to loss of kinetic energy by scattering. The fraction of scattered ions depends on the aperture size, material, shape and the ion species and energy [S1]. An upper limit to the fraction of scattered ions is given by

$$f_{\mathrm{scatt}} = \left(1 + \frac{\Delta R}{R_{\mathrm{ap}}}\right)^2 - 1 \approx \frac{2\Delta R}{R_{\mathrm{ap}}}, \tag{2}$$

where R_{ap} is the radius of the aperture and ΔR the enlargement due to ions that can penetrate the aperture and are scattered. For our system $R_{\mathrm{ap}} = 25\ \mu$m and $\Delta R \approx 5.8\,$nm (implantation depth of 5 keV N ions into a Pt aperture curved at 30^o) the fraction is $f_{\mathrm{scatt}} \approx 10^{-3}$. For the lowest energies used in our experiments the scattering fraction is reduced by an order of magnitude. In addition, the aperture is further demagnified by an electrostatic lens to 20 μm and filtered with a second 200 μm aperture right in front of the lens. This secondary aperature absorbs ions strongly scattered at the main 25 μm aperature. Thus, we expect no significant impact of aperature scattering on ion implantation depth.

2.2. Channeling

Ion channeling describes a kinetic ion "traveling" along crystal planes, resulting in a reduced number of collisions. Channeling leads to an underestimation of defect depth [S4, S7, S8]. The relevant parameters concerning ion channeling are the angle between the ion beam and the crystal planes, and ion energy. For a particular crystal orientation, only ions impinging within a certain acceptance angle can channel along crystal planes. This angle is called the critical angle. Furthermore, channeling does not occur below a certain critical kinetic energy threshold.

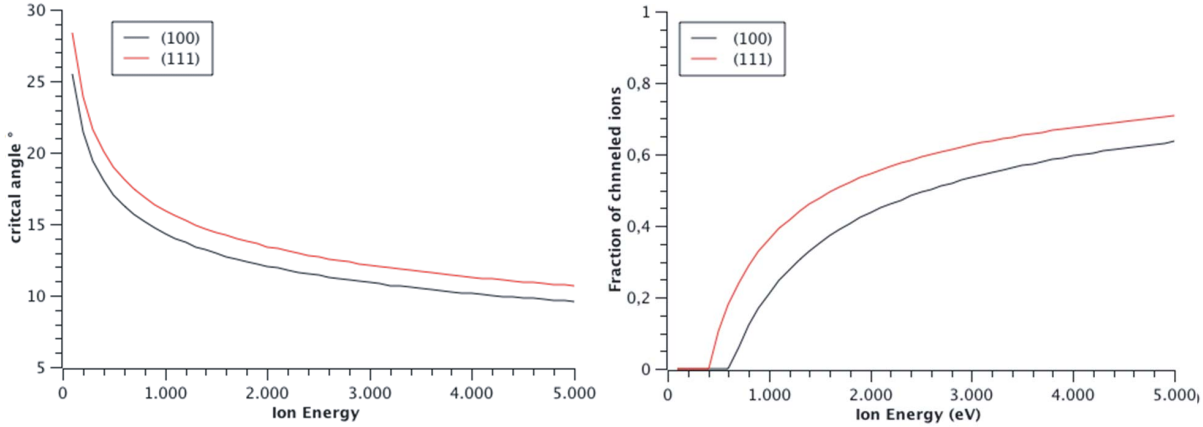

Figure C: (a) Critical angle and (b) Channeling fraction as a function of ion energy for N implantation into diamond. The critical energy is 0.6 keV for implantation into the (100) surface.

We have calculated the critical angle and critical energy for N implantation into (100)-oriented diamond based on the model by Lindhart [S9, S10]. The results of these calculations are plotted in Figure C. Fig. C(a) shows that the critical angle becomes large at low energies and channeling is

generally expected under these conditions (the incident angle in our experiment is $\pm 1^{o}$ off (100)). Fig. C(b), on the other hand, shows that the fraction of N ions undergoing channeling is reduced at low energies and is zero for ions below a critical energy. This critical energy is 0.6 keV for our case. Thus, channeling will occur for a fraction of the ions implanted at higher energy but not for the lowest energies (namely 0.4 and 0.6 keV) used in our study.

The enhancement of penetration depth for the fraction of ions undergoing channeling can only be estimated for the low kinetic energies used in our study. Secondary ion mass spectrometry (SIMS) measurements on ^{14}N ions implanted into (100) diamond at higher energies (10-30 keV) showed that the deep tail is roughly twice as deep as estimated by SRIM calculations [S4]. Complementary molecular dynamics simulations on 4 keV ^{14}N ions predicted a depth of 14 nm (vs. 6.5 nm by SRIM) for channeling ions, underlining the roughly two-fold depth enhancement [S11].

2.3. Cluster implantation

Cluster implantation is a widely used method in semiconductor industry to increase the throughput for shallow implant dopants. The molecule immediately dissociates when hitting the target surface and the energy of the atoms is given by the mass ratio of the accelerated molecule [S12]. For N_2 molecules, it is simply one half the implantation energy. The implantation depth is comparable to monomer ion implantation [S12]. However, it is known that cluster implantation reduces the channeling tail but increases the damage [S12]. Both effects can affect the yield and thus the photoluminescence signal; this might be related to the slight step in fluorescence we observe between 2.6 keV and 2.2 keV implantation spots [Fig. 1(a) in manuscript].

3. Photoluminescence measurements

Photoluminescence and ODMR measurements were carried out on the same home-built inverted confocal microscope, except for curves presented in Fig. 1(c,d), which used a standard fluorescence microscope. NV defects were excited at 532 nm and emitted photons were filtered at an effective bandwidth of 630-800 nm and collected by an avalanche photodiode. Single center emission was confirmed by photon autocorrelation measurements, ODMR measurements, and the fluorescence intensity. A 40x, NA=0.95 air objective (Olympus) was used to focus the laser on to diamond sample and collect photons. The sample was mounted to a motorized three-axis stage (Newport M-462-XYZ-SD) to navigate over the entire 2x2 surface of crystal. A stationary glass coverslip carrying a thin wire was inserted between objective and diamond sample for microwave excitation.

For selective measurements of NV^0 and NV^- emission two different sets of filters with bandwidths of 582-636 nm and 660-735 nm, respectively, were used (Fig. D). Photoluminescence spectra were also recorded for selected implantation spots to corroborate the findings from the filter measurements (Fig. E). The particular choice of filters is not entirely selective to the two charge states, and the curves shown in Fig. 1(c,d) have been corrected for the overlap of these filters with the excitation spectrum. The raw curves are shown in Fig. D. Corrected intensities were calculated using the following equation,

$$\begin{pmatrix} I_{\mathrm{NV^0}} \\ I_{\mathrm{NV^-}} \end{pmatrix} = \begin{pmatrix} 0.44 & 0.11 \\ 0.26 & 0.66 \end{pmatrix}^{-1} \cdot \begin{pmatrix} I_{582-636\mathrm{nm}} \\ I_{660-735\mathrm{nm}} \end{pmatrix}, \tag{3}$$

where the fraction of photons passing the 582-636 nm filter is 0.44 and 0.11 for NV^0 and NV^-, respectively, and the fraction of photons passing the 660-735 nm filter is 0.26 and 0.66 for NV^0 and

NV^-, respectively. Numbers are calculated from the spectra given in Ref. [S13].

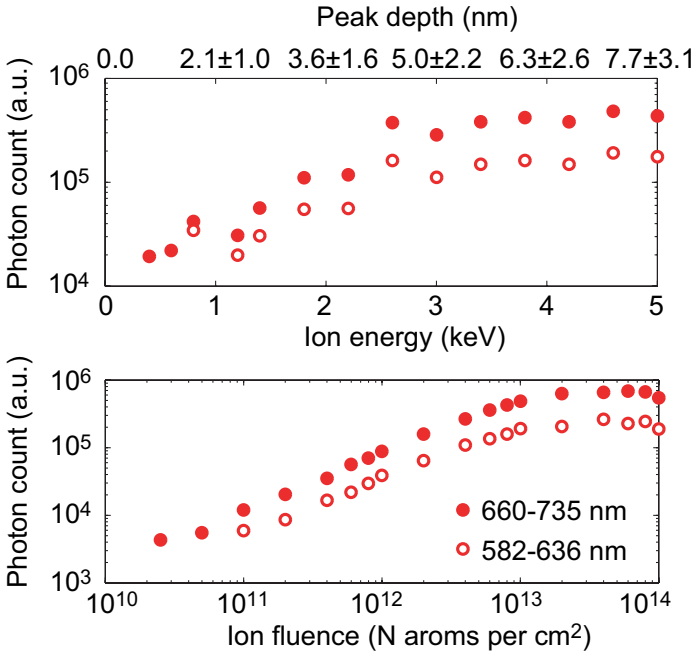

Figure D: Photoluminescence intensity versus energy and fluence, respectively, measured using two sets of filters.

Photoluminescence versus energy curves that do not discriminate between NV^0 and NV^- were also measured using the confocal setup for the fluences numbers of $8 \cdot 10^{11}\,\mathrm{cm}^{-2}$ and $1 \cdot 10^{13}\,\mathrm{cm}^{-2}$ and gave similar results.

For ODMR linewidth measurements, laser intensity and microwave power was reduced to $\sim 1\,\mu\mathrm{W}$ and a few 100 kHz Rabi frequency, respectively, to achieve linewidths of $\lesssim 1$ MHz. This linewidth is still slightly larger than those reported for intrinsically (nuclear ^{13}C spin bath) limited high-purity samples and it is likely that some residual power broadening is still present. The 1 MHz linewidth, however, is sufficient to clearly resolve the hyperfine manifold due to the nitrogen nuclear spin.

4. Line widths of ODMR spectra

4.1. Fitting of spectra

In order to determine an accurate mean number for the linewidth at various implantation energies, over 30 spectra were collected and individually fitted. The few spectra that showed a clear, extra hyperfine splitting due to proximal ^{13}C nuclei were excluded from statistics. In the vicinity of each implantation spot, ^{15}NV and ^{14}NV spectra were deliberatly taken to ensure that line broadening effects were indeed characteristic to the spot, and not to local variations in the diamond subtrate. We also measured ^{15}NV spectra at 0.4 keV for different fluences, and found good general agreement (unresolvable lines) in all of them. This indicates that there is no qualitative difference between ions implanted at different fluence and that there is no dipolar contribution to the linewidth from N donor electron spins.

Line width parameters $\Delta\omega$ (0.5× the full width at half height) for the ODMR spectra were estimated by fitting a Lorentzian to each of the hyperfine split lines. For ^{15}NV , the fit function

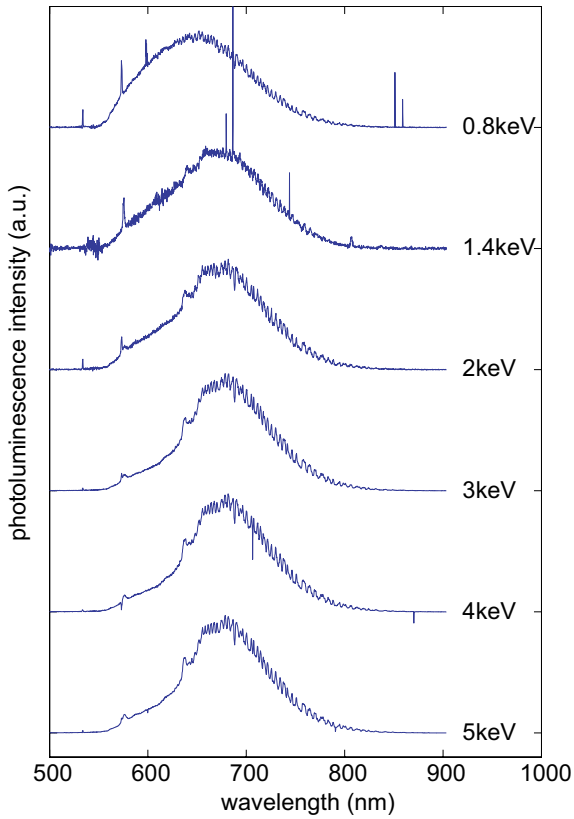

Figure E: Photoluminescence spectra of selected defects at fluence $1 \cdot 10^{13}\,\mathrm{cm}^{-2}$. Ion energy is given with each curve. Spectra are vertically offset for clarity.

used is

$$I(\omega) = I_0 - I_0 c \left[\frac{1}{\left(\frac{\omega-\omega_0+a/2}{\Delta\omega}\right)^2 + 1} + \frac{1}{\left(\frac{\omega-\omega_0-a/2}{\Delta\omega}\right)^2 + 1} \right]. \tag{4}$$

Here, ω is the microwave frequency, and I_0, c, x_0, and $\Delta\omega$ are free fit parameters that correspond to the intensity, the contrast, the center position of the ODMR line, and the linewidth (all in units of angular frequency). $a/(2\pi) = 3.0\,\mathrm{MHz}$ is the hyperfine splitting and was assumed a fixed parameter.

4.2. Calculation of the second moment close to a two-dimensional electronic spin bath

The second moment of the resonance of an electron spin S due to a quasi-continuous, two-dimensional layer of electron spins $I = 1/2$ with density ρ_A (units of spins/m^2) is given by

$$\langle \Delta\omega^2 \rangle = \frac{1}{3} \frac{\mu_0^2}{(4\pi)^2} \gamma_I^2 \gamma_S^2 \hbar^2 S(S+1) \int_{\mathrm{layer}} dx dy \rho_A \frac{(3\cos^2\theta - 1)^2}{r^6} \tag{5}$$

$$= \frac{1}{4} \frac{\mu_0^2}{(4\pi)^2} \gamma^4 \hbar^2 \int_{\mathrm{layer}} dx dy \rho_A \frac{(3\cos^2\theta - 1)^2}{r^6}, \tag{6}$$

where $\gamma_I = \gamma_S = \gamma = 2\pi \cdot 2.8 \cdot 10^{10}\,\mathrm{Hz/T}$ is the electron gyromagnetic ratio, $\mu_0 = 4\pi \cdot 10^{-7}\,\mathrm{(Vs)/(Am)}$ and r and θ the distance and angle, respectively, between the NV axis and a surface spin. This second moment has units of angular frequency squared. In the following we assume that a small bias field B_0 is applied along the NV axis and that all surface spins are aligned with this field.

For integration we note that

$$r(x,y,z) = (x^2+y^2+z^2)^{\frac{1}{2}}, \tag{7}$$

$$\cos(x,y,z) = \left[\frac{x}{r}\sin(\theta_0)+\frac{z}{r}\cos(\theta_0)\right] \tag{8}$$

where $z = d$ is the distance between spin S and the surface layer, and θ_0 is the angle between NV axis and surface normal. Integration of (6) gives

$$\langle\Delta\omega^2\rangle = \frac{1}{4}\frac{\mu_0^2\gamma^4\hbar^2}{(4\pi)^2}\frac{3\pi\rho_A[3+2\cos^2(\theta_0)+3\cos^4(\theta_0)]}{32d^4}, \tag{9}$$

$$= \frac{3\mu_0^2\rho_A\gamma^4\hbar^2[3+2\cos^2(\theta_0)+3\cos^4(\theta_0)]}{2048\pi d^4}. \tag{10}$$

For our sample, which has a (100) oriented surface, all NV spin will have the same angle set by $\cos\theta_0 = 1/\sqrt{3}$, or $\theta_0 = 54.7°$. For this angle, the second moment becomes

$$\langle\Delta\omega^2\rangle_{\theta_0=54.7°} = \frac{3\mu_0^2\rho_A\gamma^4\hbar^2}{512\pi d^4}. \tag{11}$$

4.3. Exclusion of line broadening by ^{15}N spin bath

We have also calculated the average distance between ^{15}N defects in the implanted diamond in order to exclude extra line broadening due to the N donor electron spin bath. ODMR spectra were recorded at a single fluence of $8\cdot10^{11}\,\mathrm{cm}^2$ and on defects at the perimeter of the implantation spots, where the density is reduced by about $< 1/100$ as estimated by fluorescence intensity. Peripheral defects were chosen for all measurements in order to resolve individual luminescent centers and to ensure N ions were far enough apart. From the ion density we calculate the average (median) N-N distance to $d \approx 0.5\sqrt{0.018\cdot10^{11}\,\mathrm{cm}^2} \approx 50\,\mathrm{nm}$. The dipolar interaction at this distance is about

$$\omega_\mathrm{D} \approx \frac{\mu_0}{4\pi}\frac{1}{d^3}\frac{\hbar\gamma^2}{4} \approx 2\pi\cdot100\,\mathrm{Hz}, \tag{12}$$

where γ is the electron gyromagnetic ratio. This value is much less than the base linewidth of $\sim 1\,\mathrm{MHz}$ relevant to our study.

5. Spin echo measurements and fitting of decay times

Coherence times T_2 were measured using a Hahn echo sequence with equal free evolution times $\tau' = \tau$ before and after the central π pulse. This pulse sequence produces the decay of the echo maximum. The echo decay curves were then fitted by the following equation (adapted from Ref. [S14]),

$$I(\tau) = A\exp\left[-\frac{(2\tau)^{n_1}}{T_2^3}\right]\cdot\sum_{k=0}^{N}\exp\left[-\frac{(\tau-k\tau_r)^{n_2}}{(2\tau_c)^2}\right]+C, \tag{13}$$

where τ_c describes the fast initial decay caused by the fluctuating ^{13}C nuclear spin bath, T_2 the slower decay of the "echo revivals" appearing at the periodicity τ_r of the ^{13}C Larmor precession, and $n_1 = 3$, $n_2 = 2$. Here, A, C, τ_c, T_2 and τ_r are free fit parameters, and N was adjusted to match the number of revivals seen. We also tried fitting with arbitrary exponentials n_1, n_2, but fits would either not converge or yielded the same values for τ_c and T_2 within experimental error. Thus, no

conclusion can be drawn on the exponent. In principle, the T_2 decay exponential will change from $n_1 = 3$ to $n_1 = 1$ for a rapidly fluctuating environment (such as caused by fast reorientation of surface spins), but from the present data we cannot favor one over the other.

References

[S1] J. Meijer *et al.* , Appl. Phys. A **91**, 567-571 (2008).

[S2] K. T. Koga *et al.* Phys. Earth Planet. Inter. **139**, 35-43 (2003).

[S3] A. M. Edmonds *et al.* , arXiv:1112.5757 (2011).

[S4] D. M. Toyli, C. D. Weis, G. D. Fuchs, T. Schenkel, and D. D. Awschalom, Nano Lett. **10**, 3168-3172 (2010).

[S5] Ziegler, J. F; Biersack, J. P.; Ziegler, M. D. "SRIM, the stopping and range of ions in matter", http://srim.org.

[S6] P. Honicke *et al.* , Anal. Bioanal. Chem. **396**, 2825-2832 (2010).

[S7] T. E. Derry, R. W. Fearick, and J. P. F. Sellschop, Phys. Rev. B **26**, 17-25 (1982).

[S8] R. Smith, and R. Webb, Philos. Mag. Lett. **64**, 253-260 (1991).

[S9] A. Redinger, S. Standop, Y. Rosandi, H. M. Urbassek, and T Michely, New Journal of Physics **13**, 013002 (2011).

[S10] J. Lindhard, **12**, 126-128 (1964).

[S11] Kai Nordlund, private communication.

[S12] J. H. Liang, S. L. Chiang, C. T. Chen, H. Niu, and M. S. Tseng, Nucl. Instrum. Methods B **190**, 767-771 (2002).

[S13] L. Rondin *et al.* , Phys. Rev. B **82**, 115449 (2010).

[S14] L. Childress *et al.* , Science **314**, 281 (2006).